Metastability and Structural Polymorphism in Noble Metals: The Role of Composition and Metal Atom Coordination in Mono- and Bimetallic Nanoclusters

Sergio I. Sanchez,[†] Matthew W. Small,[†] Emil S. Bozin,[‡] Jian-Guo Wen,[†] Jian-Min Zuo,[§] and Ralph G. Nuzzo[†,§,*]

[†]Department of Chemistry and the Frederick Seitz Materials Research Laboratory and [§]Department of Materials Science and Engineering, University of Illinois at Urbana—Champaign, Urbana, Illinois 61801, United States and [‡]Condensed Matter Physics and Materials Science Department, Brookhaven National Laboratory, Upton, New York 11973, United States

ABSTRACT This study examines structural variations found in the atomic ordering of different transition metal nanoparticles synthesized *via* a common, kinetically controlled protocol: reduction of an aqueous solution of metal precursor salt(s) with NaBH$_4$ at 273 K in the presence of a capping polymer ligand. These noble metal nanoparticles were characterized at the atomic scale using spherical aberration-corrected scanning transmission electron microscopy (C_s-STEM). It was found for monometallic samples that the third row, face-centered-cubic (fcc), transition metal [(3M)—Ir, Pt, and Au] particles exhibited more coherently ordered geometries than their second row, fcc, transition metal [(2M)—Rh, Pd, and Ag] analogues. The former exhibit growth habits favoring crystalline phases with specific facet structures while the latter samples are dominated by more disordered atomic arrangements that include complex systems of facets and twinning. Atomic pair distribution function (PDF) measurements further confirmed these observations, establishing that the 3M clusters exhibit longer ranged ordering than their 2M counterparts. The assembly of intracolumn bimetallic nanoparticles (Au—Ag, Pt—Pd, and Ir—Rh) using the same experimental conditions showed a strong tendency for the 3M atoms to template long-ranged, crystalline growth of 2M metal atoms extending up to over 8 nm beyond the 3M core.

KEYWORDS: nanoparticle · atomic structure · noble metals · bimetallic · core—shell · pair distribution function · aberration corrected electron microscopy

Progress in recent years has seen important advances made in nanoscience toward the development of useful new forms of nanotechnology.[1−8] One recurring theme found in research is controlling structures with nanometer precision.[9−12] The difficulty with synthesizing ever-smaller structures is that the outcome of a reaction is dictated by a complex interplay of thermodynamics and kinetics. Kinetically favored products may or may not be the same as those preferred thermodynamically. Under different conditions the most stable structure of a material may in fact also be size-dependent and change from a single-crystalline habit to one that exhibits twinning or is amorphous.[13,14] Because of this, and the broader utility of crafting structures at the atomic scale, it is imperative to understand both kinetic and thermodynamic contributions to materials synthesis.

It is now well understood that catalytic properties of nanoscale metal clusters depend markedly on the structure of their exposed surfaces.[15−18] Vertex and edge atom sites are known to bind more strongly to molecules and reactive intermediates, doing so in ways that broadly impact reaction rates.[19−21] A notable study by Bratlie *et al.*[15] demonstrated that different nanocrystal morphologies can wholly dictate the outcome of a prototypical catalytic reaction. Cubic Pt crystals defined by {100} planes, for example, are selective for the hydrogenation of benzene to cyclohexane,

* Address corrrespondence to r-nuzzo@illinois.edu.

Received for review November 15, 2012 and accepted December 28, 2012.

10.1021/nn305314m

while cuboctahedral structures (defined by {100} and {111} planes) yield a mixture of cyclohexene and cyclohexane under similar conditions.[15] Such data motivate this work to better understand the factors that control nanocrystal growth.

Research has shown that different avenues exist by which materials growth chemistry can generate desired nanostructures.[22] The stabilities of structures produced using chemically controlled procedures can vary in complex ways depending on size and the presence of other species.[18,22−27] Theoretical calculations, predict that fcc, single-crystalline nanoparticles will assume a truncated octahedron confined by the {111} and {100} families of planes as their equilibrium thermodynamic shape.[24] The formation of such a shape, however, embeds costly energetic motifs due to the presence of undercoordinated atoms.[28] Conversely, particles not composed of a single crystal domain (and therefore containing multiple twins) adopt an icosahedral or decahedral crystal morphology, where the faceting is exclusively defined by low energy {111} terminating facets.[28] Ultimately, it is these planes that assist in the formation of a low energy structure, albeit at the cost of increased internal strain.[13,23,28] In these scenarios the mediating effects of surface energy dictate the nanoparticle's stable geometry. Theoretical calculations predict that a crystal bound by high index crystal planes will ultimately minimize the surface energy by reconstructing and assuming more favorable, lower index faceting, namely, the {111}, {100}, and {110} families of planes.[22,23]

The energetic driving force for the reconstruction to lower index planes arises from the instability associated with undercoordinated atoms.[29,30] With nanoparticles this behavior is complicated by the curvature adopted to minimize the exposed surface area. Creating a rounded structure from a collection of facets inevitably applies increased strain to atoms residing at the edges and vertices of adjoining crystal planes.[19,31−33] Because these atoms have fewer neighbors than those situated on a flat surface, the coordination environment is more extreme.[19,31] As a result, they have more unsatisfied bonds and are less stable.[31−33] In discriminating the different surface truncation energies, it is easy to see why a high atomic density (111) surface is intrinsically more stable than a lower atomic density (100) surface.[34]

Despite the significant role thermodynamics plays in directing the attributes of nanostructures, kinetics cannot be neglected as a complex and often competing contributor. It is frequently found that adjusting experimental parameters (*i.e.*, capping agent, reducing agent, temperature, *etc.*) can yield products with specific morphological features,[2,3,22,35,36] crystal sizes,[3,22,37−39] and catalytic activity.[25−27,40−43] In such cases the geometry of a nanocrystal is not solely determined by the minimization of its surface energy (thermodynamic minimum). Instead one must consider the possible formation of metastable structures possessing a conversion potential well too deep to overcome.[13,24] In such cases, the reactions result in the formation of thermodynamically unfavorable features.[23] Therefore a balance exists in that the metastable structure formed may reside far away from the global energetic minimum.

We report the results of an investigation of the synthesis of polyvinylpyrrolidone (PVP) capped nanoparticles grown in solution from six noble metal precursors (Rh, Pd, Ag, Ir, Pt, Au) using $NaBH_4$ as a reducing agent. Because of the high reduction potential of $NaBH_4$, this growth is very rapid, proceeding from a burst of nucleation events and is known to produce a large number of very small nanoparticles (∼1 nm).[44] Generally speaking, the synthetic approach illustrates growth occurring under conditions of kinetic control. Our results show clear structural differences between the 2 and 3M nanostructures investigated that cannot be explained merely by thermodynamic arguments and indicates that there is a distinct, electronic structural sensitivity. Using C_s-STEM we characterize the atomistic details that differentiate the 2 and 3M nanoparticle structures formed and define size-dependent patterns related to their stability. Conclusions supported by the C_s-STEM data agree fully with measurements made using high-energy X-ray diffraction (XRD). The latter XRD data confirm that a dilation of the lattice constant occurs for the 2M nanoparticles whereas the 3M series presents more bulk-like values. We further compare the PDF measurements to assess the levels of coherence/crystallinity present in these materials. Most revealing are features observed for the intracolumn bimetallic (Au−Ag, Pt−Pd, and Ir−Rh) structures, where the 3M metal atoms of a growth-nucleating core impart their bonding structure onto 2M atoms in core−shell habits to very large cluster diameters—essentially directing the overall growth of the 2M atoms—whereas without their presence disordered crystal morphologies dominate.

RESULTS AND DISCUSSION

Structural and Crystallographic Analysis of Single-Element Nanocrystals. Figure 1 shows representative C_s-STEM micrographs of metals in the 3M series of nanocrystals (Au, Pt, and Ir). The Au samples (Figure 1a−c), for the synthetic protocols used here, presented with a relatively wide distribution of particle sizes (2.2 ± 1.7 nm; Supporting Information (S.I.) Figure 1) with some appearing single crystalline and others being symmetrically twinned (S.I. Figure 2). Although only single crystals are depicted in Figure 1, it was generally observed that both the single and polycrystalline particles revealed an atomic structure in which Au atoms could be identified up to the terminating edges. Fast Fourier transforms (FFTs) of the micrographs

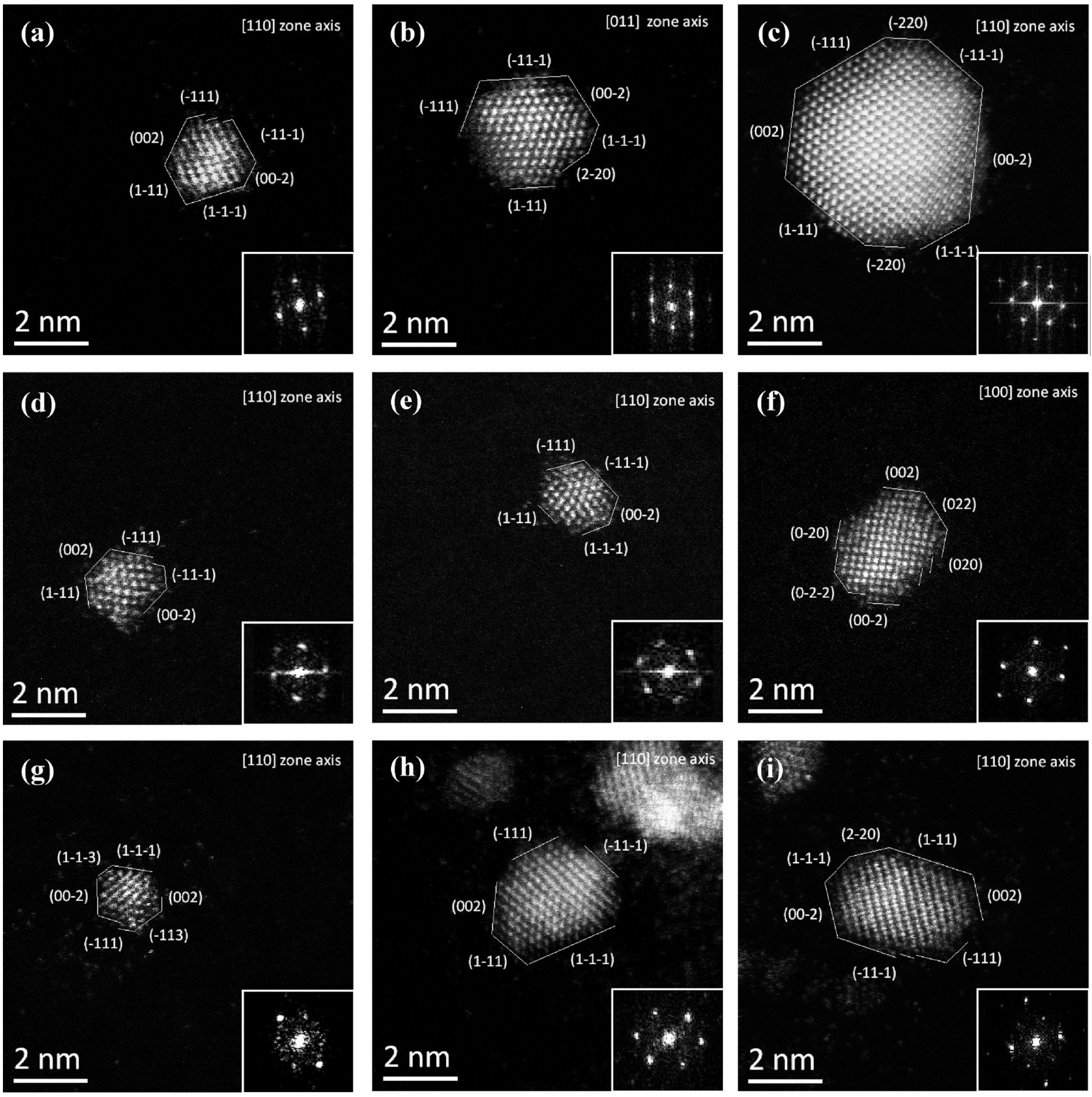

Figure 1. Representative C$_s$-STEM micrographs of the 3M nanocrystals, Au (a–c), Pt (d–f), Ir (g–i). Facets and crystal orientation corresponding to the inset FFT are annotated directly on the micrographs.

(*i.e.*, the power spectra) are given as insets in the lower right of Figure 1a–c. The spatial frequencies associated with the periodic placement of atoms in the crystal make it possible to identify the zone axis of the cluster and index their bounding facet structure. This analysis was easier to carry out for larger crystals within the size distribution since they were more frequently found to be crystalline. In addition to identifying an approximate zone axis, the FFT also made it possible to determine an apparent lattice constant for the Au particles (4.05 ± 0.12 Å, in close agreement with the literature value of 4.08 Å for bulk Au).[45] The values obtained using the FFT tend to lack high precision because nanocrystals are rarely perfectly oriented along a zone axis and for this reason many of these projection-limited values must be averaged. Table 1 shows that with adequate sampling the lattice constants so deduced can still be accurate—in the present work the values so obtained for all metals investigated were found to compare very favorably with bulk reference values. As expected, low-index planes define a common feature of the crystals' facet structures.[16]

Figure 1d–f shows representative images of Pt nanocrystals taken from a sample with a size distribution of 1.5 ± 0.6 nm (S.I. Figure 1). The atomic ordering evident within the images allowed lattice parameters and facet structures for these nanocrystals to be assigned. An estimated lattice parameter of 3.90 ± 0.09 Å closely matches the literature value of 3.92 Å for bulk Pt (Table 1).[45] Unlike Au, which exhibited frequent twinning, the Pt samples were predominantly single-crystalline.

The Ir specimens (Figure 1g–i) resemble the Pt samples with the exception of being highly susceptible to aggregation (not sintering). Although the mean particle size (1.6 ± 0.8 nm, S.I. Figure 1) was on the

TABLE 1. Comparison of Lattice Parameters Determined by C_s-STEM and High-Energy XRD Tabulated with Literature Values

	lattice constants		
element	microscopy – experimental value (Å)	X-ray diffraction – experimental value (Å)	literature value (Å)
Ag	4.16 ± 0.05^a	4.12 ± 0.06	4.09
Au	4.05 ± 0.12	4.05 ± 0.02	4.08
Pt	3.90 ± 0.09	3.92 ± 0.05	3.92
Pd	4.00 ± 0.15	3.95 ± 0.04	3.89
Ir	3.84 ± 0.09	3.84 ± 0.13	3.84
Rh	3.90 ± 0.19	3.89 ± 0.16^b	3.80

[a] The apparent disorder exhibited by the majority of Ag particles limited the amount of sampling for analysis by microscopy. [b] The Rh XRD data only presented two discernible Bragg peaks with which to calculate the lattice constant (the (200) and the (333)) peaks.

order of Pt and Au, Ir particles were seldomly found in isolation. As with the other 3M metals, the Ir nanocrystals bounding edges were often assignable using the spectral data from the FFT of the image. Surprisingly, unlike the other 3M structures, Ir crystals experienced an increase in twinning defects at larger sizes (S.I. Figure 3). As shown in Table 1, our analysis indicates an average lattice parameter of 3.84 ± 0.09 nm for the Ir clusters, in agreement with that of bulk fcc Ir (3.84 Å).[45]

Figure 2 shows a collection of C_s-STEM micrographs for the 2M (Ag, Pd, and Rh) nanoparticles. Dimensional analysis of the Ag nanoparticles revealed a mean particle diameter of 3.4 ± 2.8 nm (S.I. Figure 1), thus allowing a broad distribution of cluster sizes to be structurally characterized. With few exceptions, the Ag particles observed appeared highly disordered, lacking both well-defined boundaries and long-ranged atomic periodicity (Figure 2a–c). In contrast to the 3M specimens, C_s-STEM imaging of the Ag samples revealed no apparent correlation between size and the emergence of a more ordered habit over the particle sizes present. The absence of spatial frequencies in the power spectra (inset in the Ag nanocrystal micrographs) supports this finding, where the presence of a bright ring is generally found in place of distinct spatial frequencies. As in diffraction, a sharp ring structure would indicate a polycrystalline material (here all contributing crystals are within a single image) and an increasing diffuse component in the ring(s) indicates a move toward an amorphous structure. Given the disorder present in this sample, only a limited number of clusters provided the structural information given in Table 1.

Imaging of the Pd specimens (Figure 2d–f; 1.6 ± 0.8 nm, S.I. Figure 1) also revealed the presence of a generalized trend toward structures that looked more disordered. Unlike the case for Ag, Pd nanoclusters strongly evidenced size-dependent behavior. Increasing cluster sizes led to a propensity for adoption of an ordered habit. The ordering seen, however, was not generally found to be associated with single crystals until reaching relatively large sizes (as illustrated by representative examples shown in Figure 2d–f). Most strikingly, we found no examples in which Pd particles smaller than ~3 nm exhibited crystallographic data amenable to the assignment of a single lattice, although this does not rule out their existence. Nonetheless, the trends observed *via* electron microscopy and the absence of crystalline Pd particles below 3 nm in a multitude of images surveyed indicate that they must be rare. Interestingly, the observation of significant twinning within these structures agrees with results from our previous work[46] even though the synthesis methods differ.

Structural properties similar to Pd were observed for the Rh nanocrystals (1.5 ± 0.5 nm, S.I. Figure 1). Smaller Rh crystals (<2.6 nm) were not found to adopt geometries with an organized packing structure. They appeared as collapsed clusters of atoms showing no evidence of the spatial frequencies expected for an fcc crystal (Figure 2g,h). Particles exceeding this apparent threshold limit began to display evidence of crystallinity, as revealed in the FFT data. Multigrained nanoparticles were often found in which multiple crystal domains could be observed. It is clear that, for both the 2 and 3M clusters, there exist size-dependent variances in metal atom bonding that affect the final level of disorder.

Lattice constants calculated for the 2M samples, as determined by microscopy, are listed in Table 1 for the Ag, Pd and Rh nanoclusters. A comparison with literature values (Table 1) reveals a trend toward dilation of the lattice constants for these three samples with respect to their values in bulk. The fact that tensile (noncompressive) strains are present is very surprising, and contrasts with the common notion of surface atom relaxation in the atomic structures of metal nanoparticles.[29,30] In this regard the 2 and 3M series of metals are very different. For the case of Au, Pt, and Ir, the atomically resolved micrographs show bonding comparable to the bulk. Both the Pt and Au nanocrystals, as might be expected, seem to show slight relaxations of their lattice parameters based on the microscopy.

Unfortunately, electron microscopy only provides a localized description of the features observed for the overall specimen. To verify that the trends observed

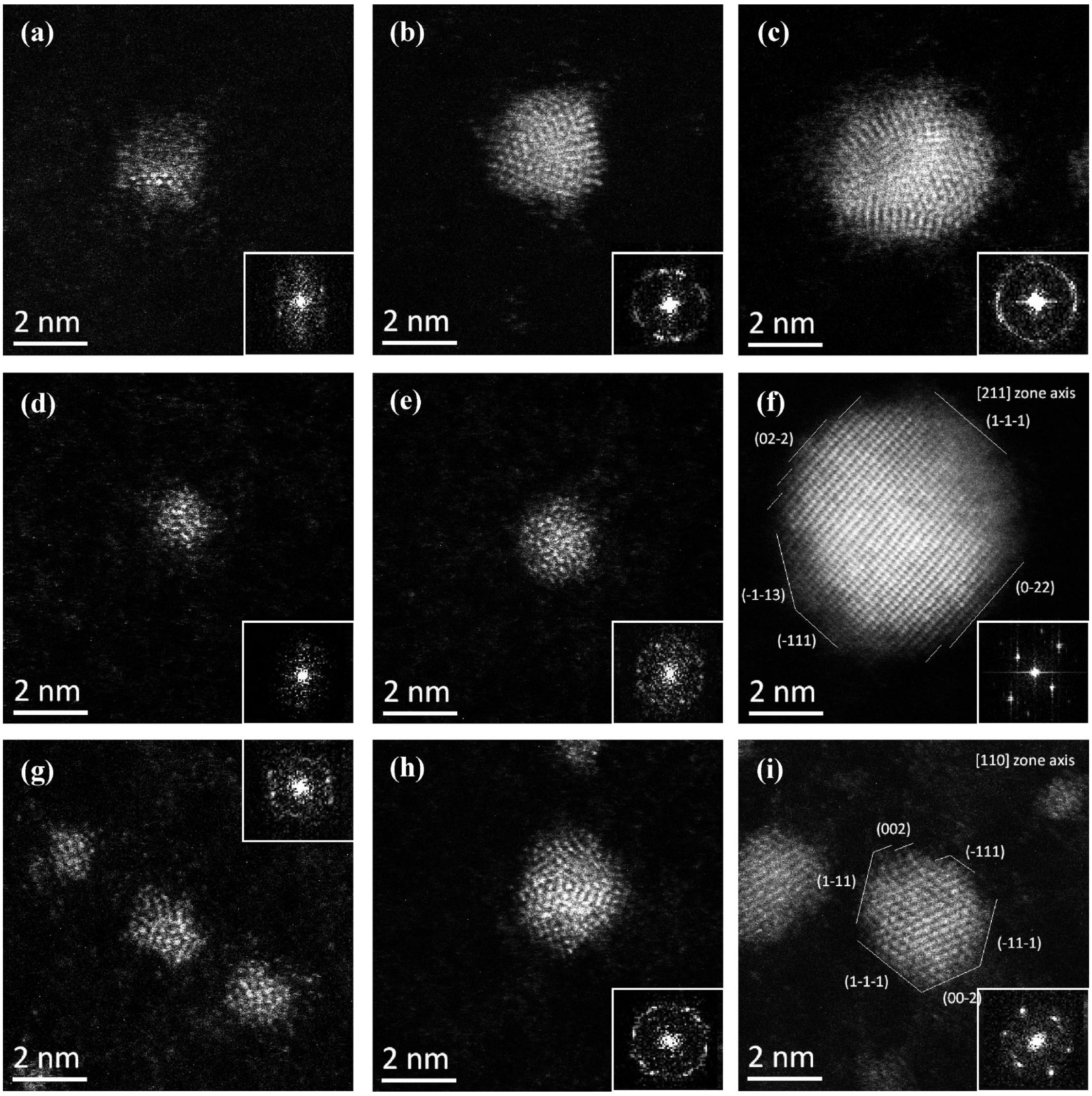

Figure 2. Representative C_s-STEM micrographs of the 2M nanocrystals, Ag (a–c), Pd (d–f), Rh (g–i). Facets and crystal orientation are annotated only in instances where the nanocrystal and inset FFT indicated a faceting structure.

are not caused by selective sampling, a bulk analytical technique was used to provide independent analysis and support the structural interpretations reached above. Data from high-energy XRD measurements were collected to provide a comprehensive structural assessment of the samples. Lattice parameters were determined from the Bragg peak reflections in the diffraction profiles and are presented in Table 1. A comparison of the lattice constants from the XRD measurements with those obtained from C_s-STEM shows close agreement. Significantly, the trend in which small 2M clusters exhibit a dilation of their lattice parameters compared to those bulk materials was reaffirmed. On the basis of the XRD data, the Ag, Pd, and Rh nanoparticles all have average lattice constants showing slight tensile strains in agreement with the values deduced *via* microscopy. Similar findings have been reported in other studies of Ag,[47] Pd,[48−51] and Rh[51] nanoparticles. These studies attributed the observed strains to changes in structure that result variously because of the surrounding medium,[47] the presence of low-coordination number surface atoms,[51] and the disorder of surface atoms.[48] The C_s-STEM data support a comprehensive structural feature embracing such attributes, but with a more complex underpinning. More specifically, the inability to terminate the 2M nanocrystal surfaces with well-defined facets may induce a tensile strain in the core atoms as they attempt to accommodate the disorder present at the surface.[48]

At this point it is important to define what structural features are encompassed by the term "disorder" in the context of this study. Although it was mentioned that some of the particles undergo twinning (*e.g.*, Au, Ir, Rh, *etc.*) this does not preclude the possibility of forming definable planes (S.I. Figure 2 and 3). In the same

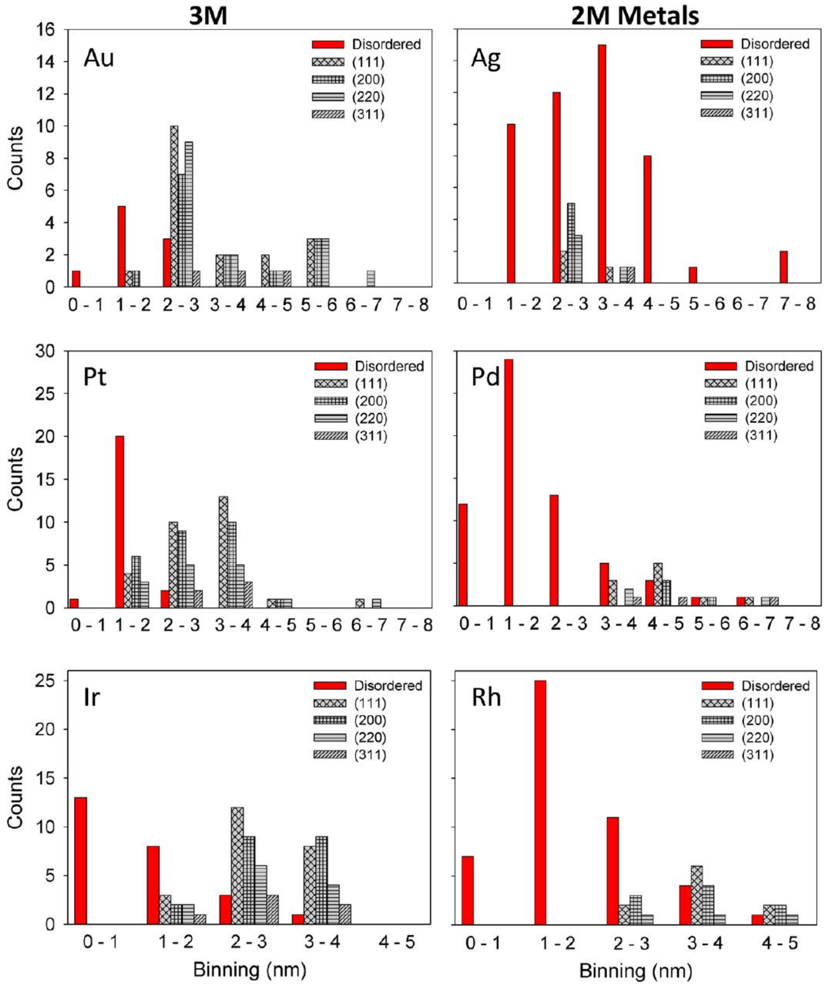

Figure 3. Binned histograms defining the size-dependent nature of crystallinity for the 3M (Au, Pt, Ir) and 2M (Ag, Pd, Rh) metals. The red bars represent "disordered" clusters such that atomically resolved images showed no extended structure across the particle. The hatched bars tally the frequency of crystal planes defined by FFT. Note: The frequencies of the binned data do not reflect the size distributions of the samples.

respect, a particle may exhibit crystallinity at the core even if the periodic nature of the atom packing does not extend to its surface. By "disordered" nanoparticles we refer to an organization of the atoms such that an extended, periodic packing structure is not present in the cluster. These are, in effect, amorphous states that embed large strains. The power spectra of such disordered clusters will not exhibit the spatial frequencies expected for an ordered habit and yield an amorphous pattern due to the disorder present. Nevertheless, interpretation of such "disorder" should be undertaken cautiously since even crystalline clusters along non-zone axes may exhibit projections that satisfy the above criterion.

To better understand if the microscopy results were truly indicating disorder we examined a large number of clusters for each sample. If no preferred orientation exists, all the samples should present equivalent rates of crystalline/disordered structures. Figure 3 presents the frequency of exposed surfaces (*e.g.*, the (111), (200), *etc.*) occurring for each sample as well as the abundance of disordered particles (lacking any observable lattice structure) quantified and binned with respect to size (*e.g.*, 0−1, 1−2, 2−3 nm, *etc.*). One notes that the occurrence of definable planes is strongly related to particle size for the 3M specimens. Below particle sizes of ∼1 nm there were no clusters for which such assignments could be made. In the 1−2 nm regime, however, the onset of crystallinity is noted by the emergence of well-defined truncating planes. With increasing size of the 3M nanocrystals, the presence of the {111}, {100}, {110}, and {311} family of planes becomes more numerous and ultimately dominates the observed crystal geometries. The behaviors for the 2M structures are more complex and show an extended range in which disordered morphologies prevail. The Ag nanoclusters showed no size-dependent crystallinity as noted by the abundant distribution of disordered particles throughout the binned data. The Pd and Rh clusters exhibited a more conventional behavior with disordered structures becoming less common for larger particles. The onset of ordering in the 2M samples appears to occur most prominently in the size range between 2 and 4 nm. Even so, disordered particle habits persist to very large sizes (*e.g.*, Rh (4−5 nm), Pd (6−7 nm), and Ag (7−8 nm)), values much larger than is seen for their 3M counterparts (*e.g.*, Ir (3−4 nm), Pt (2−3 nm), and Au (2−3 nm)).

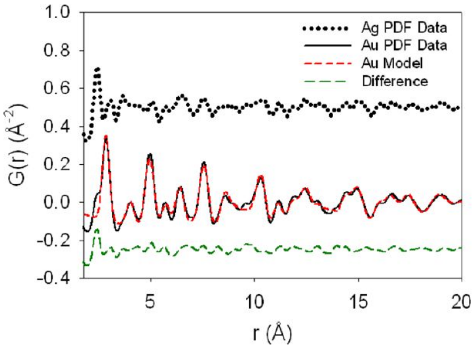

Figure 4. Atomic PDFs comparing Au (solid black line) and Ag (dotted line), with the Ag profile vertically displaced by +0.5 Å^{-2} for clarity. The red curve is the fit modeling the experimental PDF data to a spherically shaped fcc Au crystal. The difference profile (green curve) between the experimental data and fit is vertically displaced by −0.25 Å^{-2}.

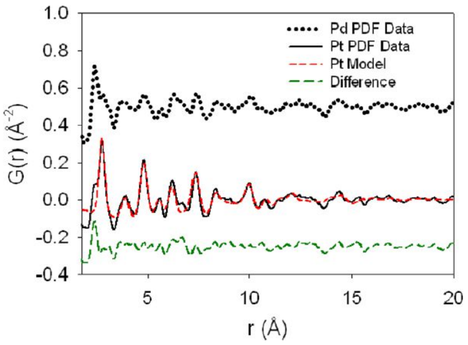

Figure 5. Atomic PDFs comparing Pt (solid black line) and Pd (dotted line), with the Pd profile vertically displaced by +0.5 Å^{-2} for clarity. The red curve is the fit modeling the experimental PDF data to a spherically shaped fcc Pt crystal. The difference profile (green curve) between the experimental data and fit is vertically displaced by −0.25 Å^{-2}.

Atomic PDF Analysis of Single-Element Nanocrystals. To ensure that the nature of the observed structural features in the 2 and 3M series can be interpreted in terms of crystallinity, we employed a total X-ray scattering based PDF technique.[52−54] Since the PDF includes both Bragg peaks and the diffuse components of the diffraction pattern, its Fourier transform reflects both the local and average atomic structure. It is particularly sensitive to the atomic short-ranged ordering since the scattered intensities are weighted by the magnitude of their wave vectors. This makes the PDF method suitable for characterizing materials in cases where deviations from the average structure are present, such as aperiodic distortions in bulk crystal structures, nanoporous materials, and, most importantly here, finite-size, nanomaterial systems.[52,53]

Figures 4−6 show the atomic PDF results for the six monometallic samples examined in our study. Comparing the PDFs of the 2 and 3M nanoparticles it is immediately evident that there exists a difference in the long-range order of the atom pair distances. Figure 4 directly compares the measured PDFs for the specific case of Au and Ag. The Au PDF displays multiple peaks at specific atom-pair distances extending beyond 20 Å, a value consistent with the mean particle size of the Au clusters (2.2 nm). Conversely, the PDF for Ag (dashed black line) lacks any features with significant intensity denoting recurrent atom pair distances being present in the sample. This observation is somewhat surprising considering the average particle size of the Ag specimen (3.4 nm) would lead one to expect more bulk-like structural features in clusters of this size (*i.e.*, long-ranged order, well-defined, intense pair-distance peaks, *etc.*). The lack of well-defined atom-pair contributions for the Ag samples precluded PDF modeling. The Au PDF data, however, allowed full modeling, as shown by the red curve overlying the experimental data (solid black line) in Figure 4. The structural model used in this fit was that of bulk Au, conforming to $Fm\bar{3}m$ space group constraints. Assuming a spherical particle, a spherical shape-function envelope was used to account for the effects of the

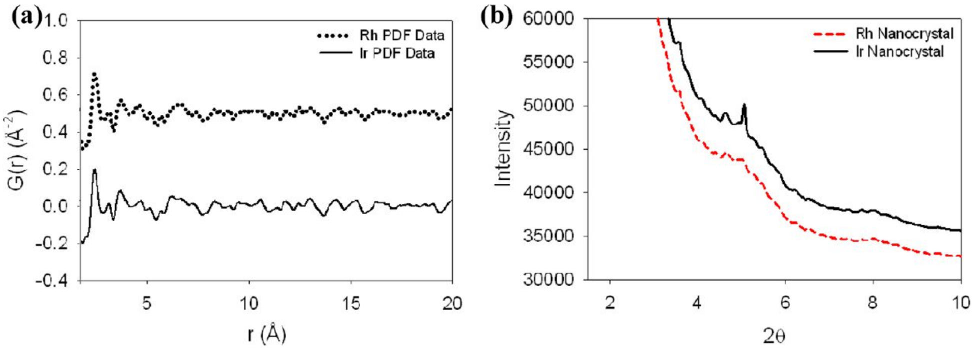

Figure 6. (a) Atomic PDFs comparing Ir (solid black line) and Rh (dotted line), with the Ir profile vertically displaced by +0.5 Å^{-2} for clarity. (b) Un-normalized raw XRD data showing the presence of Bragg reflections in the Ir data and correspondingly absent in the Rh data.

nanoparticle's finite dimensions on the PDF profile. The model structure indicated an fcc Au particle measuring 2.8 ± 0.1 nm in diameter, a value consistent with the microscopy data for this sample (2.3 ± 1.7 nm, S.I. Figure 1). The lattice parameter deduced from the fit was 4.06 ± 0.01 Å, also in excellent agreement with the microscopy and XRD findings (Table 1).

The data in Figure 5 compare the PDFs collected for the Pt and Pd samples. The Pt crystals produced multiple peaks at specific atom-pair distances extending to ~14 Å. The resolvable peak intensities for the Pt data (solid black line) allowed modeling of the PDF (solid red line). Similar to the case of the Au nanocrystals, a best fit was obtained for the Pt nanocrystals by refining a structure based on that of bulk Pt. A spherically shaped particle morphology was again assumed, and a spherical shape-function envelope used while considering the constraints imposed by the $Fm\bar{3}m$ space group symmetry. The particle diameter of 1.8 ± 0.1 nm calculated from the model closely matches the results obtained by microscopy (1.5 ± 0.6 nm). The lattice parameter obtained was 3.93 ± 0.01 Å, again in close agreement with the data in Table 1. The PDF of the Pd nanocrystals extends to 1.6 nm and shows lower intensity peaks (dashed black line) and less coherence with increasing *r*. As with the Ag data, the weaker Pd signal precludes analysis beyond assignments providing qualitative agreement with the trends observed by microscopy. It is also worth mentioning that past studies assessing the atomic structure of Pd nanoparticles using atomic PDFs also show that significant levels of disorder are present in clusters of this size.[55]

The Ir and Rh data produced more complex PDF patterns than were observed for any of the other samples (Figure 6a). Although not obvious in the PDFs, the raw XRD data (Figure 6b) unambiguously shows that the Ir nanocrystals yield more intense Bragg reflections than is seen for the Rh clusters. Even so, the data in each case precluded analysis by fitting the PDF function. On the basis of the microscopy data alone, we conclude that Ir nanoclusters are the least crystalline of the 3M metals (notably because of the significance of twinning), yet have a more coherent atomic bonding structure than its similarly sized 2M analogue.

Kinetic Analysis of the Nanocrystal Synthesis. We next considered the importance of metastable states that result from the methods of synthesis used. To do so we synthesized samples using two different methods, with one proceeding at elevated temperatures. The only similarities between the methods used were the metals investigated and the use of PVP as the capping agent. Our first procedure is based on the protocol of Tsunoyama *et al.*[56] and uses rapid reduction to produce nanomaterials with reasonably well controlled dimensions at 273 K (see Experimental Methods, Preparation of Nanocrystals). The second method used a softer reduction, where an ethylene glycol solution containing a metal salt and PVP was heated to over 415 K (S.I. Experimental Details). This should result in more thermodynamically controlled structures since the reduction proceeds more slowly and the higher temperatures allow the clusters to sample a larger structural phase space.[57] Despite these differences, no significant impacts on the structural trends were observed for the samples investigated (monometallic samples only, S.I. Figures 4 and 5). The results confirmed the structural behavior of Pt and Pd described in a previous study using C_s-STEM and XRD.[46]

Chemical and Crystallographic Analysis of Binary Nanocrystals. We conducted a simultaneous reduction of neighboring metal atoms (Au–Ag, Pt–Pd, and Ir–Rh) to form intracolumn, bimetallic particles. Figure 7a shows

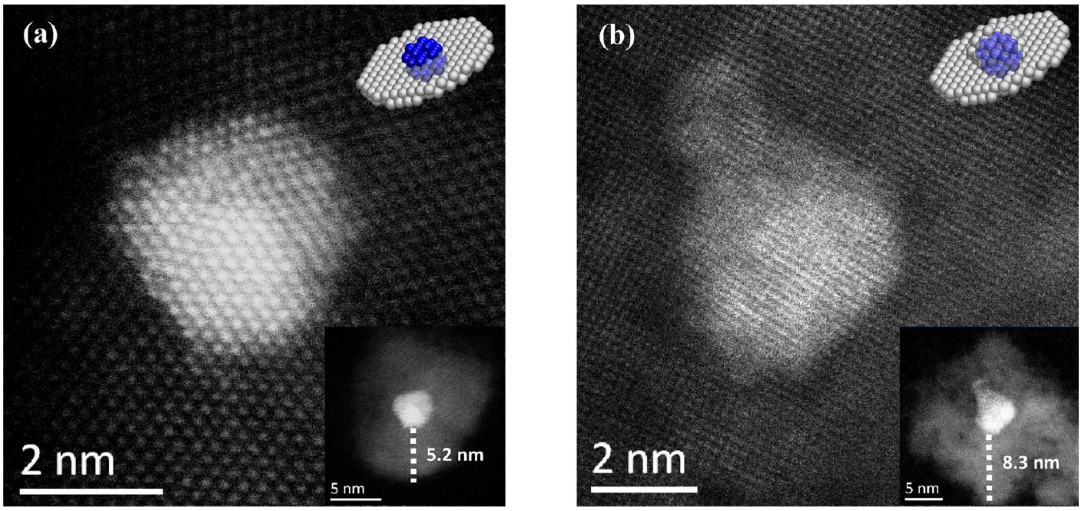

Figure 7. C_s-STEM micrographs of the bimetallic (a) Au–Ag and (b) Pt–Pd nanocrystals showing the organized atomic structure of the 2M metals (Ag and Pd) in the presence of their 3M counterparts (Au and Pt). Lower magnification images are inset in the lower right and a schematic illustration is inset on the top right. The dashed lines in the insets illustrate the extent to which the 2M metal atoms grow from the high-*Z* scattering 3M cluster.

that the combination of Au and Ag forms a phase-segregated structure. Energy dispersive X-ray spectroscopy (EDX) measurements indicated the presence of both Au and Ag in the individual nanoparticles (S.I. Figure 6a). In addition, the *Z*-contrast (achieved as a function of Rutherford scattering[58]) allows discrimination of the Au and Ag enriched regions. The high intensity regions of the micrograph are due to a predominance of Au (Z_{Au} = 79) atoms while the less intense regions are due principally to Ag (Z_{Ag} = 47) atoms. Similar qualitative analytical schemes have been observed and applied in other systems.[46,59,60] The bimetallic Pt–Pd nanocrystals (Figure 7b) show similar intensity patterns in the micrograph, where the high scattering element (Pt) was concentrated at the core and surrounded by lower scattering Pd atoms. EDX measurements further confirmed the presence of both species (S.I. Figure 6b).

Although these phase-segregated structures were frequently observed in the Au–Ag system, alloyed clusters were also found to be present (S.I. Figure 7). Interestingly, FFT analysis of the sample indicated two sets of lattice values despite the apparent coherency in the packing of the atoms. Evaluation of data from the high contrast region containing the Au core yielded a lattice parameter of 4.07 ± 0.05 Å, consistent with the quantities obtained for the monometallic Au nanocrystals (Table 1). The power spectra acquired in the low contrast regions yielded an average value of 4.14 ± 0.01 Å, closely matching the expanded lattice value determined by microscopy for monometallic Ag. Using the same FFT analysis on the homogeneously mixed Au–Ag alloys (S.I. Figure 7) a mean lattice parameter of 4.05 ± 0.03 Å was found. This latter measurement further supports the assertion that the Ag atoms adopt the bonding habits of Au atoms when the metals are combined.

The bimetallic Pt–Pd crystals formed a series of phase-segregated structures analogous to those observed for the Au–Ag specimens (Figure 7b and S.I. Figure 8). The Pd atoms are arranged periodically radiating away from the nucleating Pt center to distances that can exceed 8 nm (inset of Figure 7b). The lattice constants, as determined from the micrograph, were ∼3.92 ± 0.04 Å and an abnormally high 4.09 ± 0.05 Å, corresponding to the high-*Z* and low-*Z* regions of the micrograph, respectively. The lattice value for the high-*Z* region was in line with expectations for Pt (Table 1). For the surrounding Pd atoms, however, the calculated lattice parameter far exceeded literature values for bulk Pd as well as the experimental values obtained here for the monometallic Pd nanoclusters (Table 1).

Contrary to the phase-segregated structures observed for Pt–Pd and Au–Ag, the Ir–Rh specimens exhibited only homogeneously mixed nanocrystals (S.I. Figure 9). EDX measurements confirmed the presence of both Ir and Rh within individual nanoparticles indiscriminate of cluster size. Examination of multiple images demonstrated that the qualitative features of monometallic Ir nanocrystals are prominent despite the presence of Rh atoms. Most notably, the tendency of the bimetallic nanocrystals to form a defined crystal structure at sizes below 2 nm is observed (S.I. Figure 9), with twinning emerging as the particle sizes increased. FFT analysis of the Ir–Rh crystals revealed a lattice parameter of 3.84 ± 0.12 Å. Despite the high uncertainty associated with the approximation, it does agree favorably with the lattice constant of the monometallic Ir nanocrystals (Table 1). Although the Ir–Rh system does not generate the same phase-segregated nanostructures as the Pt–Pd or Ag–Au systems, the data do re-emphasize that the presence of 3M atoms strongly affects the bonding structure exhibited by the binary composition nanocrystal.

Atomic PDF Analysis of Binary Nanocrystals. Detailed PDF modeling was carried out to shed further light on the nature of atomic bonding present in select binary compositions. Figure 8a shows the comparison in PDF profiles between the monometallic Au and the Au–Ag data (vertically shifted by $+3$ Å^{-2}). The arrows indicate the emergence of resolvable peaks in the bimetallic

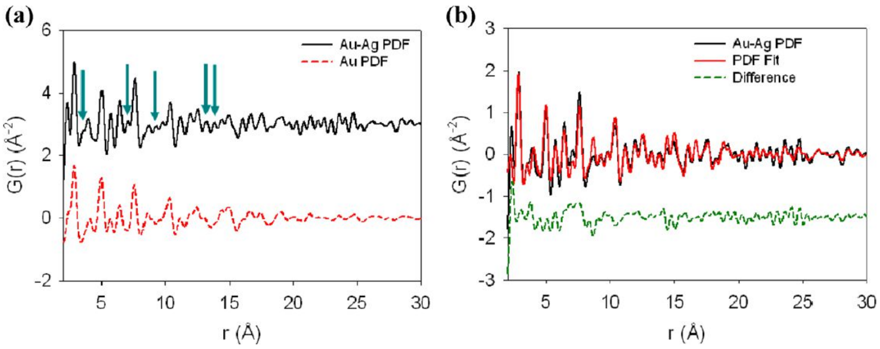

Figure 8. (a) Comparison of the atomic PDFs for the bimetallic Au–Ag (vertically displaced by $+3$ Å^{-2}) and the monometallic Au samples. Arrows in the bimetallic PDF highlight the emergence of new atom-pair contributions to the Au–Ag profile. (b) The experimental PDF data for the Au–Ag nanocrystals (in black) is modeled (in red) with a difference profile also shown (in green, vertically displaced by -1.5 Å^{-2}).

sample. This indicates the attendant contributions from separate atom-pair distances not found in the elementally pure Au system, which in this case can be ascribed to the presence of Au–Ag atom pairs.

Atomic PDF modeling is essential to elucidate the role of Ag in the Au–Ag PDF profile. Although the structure in Figure 7a suggests a phase-segregated nanoparticle habit, alloy structures were also observed, necessitating consideration of both motifs during the PDF analysis. Of the two structures, PDF modeling indicated a slight preference for the formation of a biphasic system. From a more qualitative standpoint, the data indicate that the amorphous-like packing observed for the monometallic Ag is no longer present. Instead, the analysis revealed a well-ordered material analyzable using a two-phase refinement, where the model considers the crystal structure and relative scale while assuming a 1:1 ratio of each metal. The resultant fit with a two-phase model system is shown in Figure 8b accompanied by the difference profile.

The modeling results afforded measurements of the lattice parameters for both metallic species. For the Au phase a lattice constant of 4.04 ± 0.02 Å was found, whereas the Ag phase is characterized by a lattice spacing of 4.09 ± 0.02 Å. These values agree favorably with those of bulk Ag and Au (Table 1, 4.09 and 4.08 Å, respectively). The experimental results for the Au phase in this case suggest a compressive strain is present. The fit results indicated a mean particle diameter for the clusters of 5.3 ± 0.2 nm. This value is surprising since microscopy suggests an average diameter of 12.6 ± 4.8 nm if the low-*Z* element is included. Interestingly, if only the diameter of the high-*Z* component is considered, the mean particle diameter shrinks to 5.6 ± 1.4 nm and more closely matches the value deduced in the PDF modeling.

Comparison between the monometallic Pt and the bimetallic Pt–Pd specimens revealed multiple pair distances unassignable to bulk, fcc Pt, indicated by the arrows in Figure 9a. As with the Au–Ag system, these aberrant peaks are assigned to bimetallic, Pt–Pd, bonding. As in the earlier case, using a two-phase system for the PDF modeling (Figure 9b) produced a quality fit. Lattice constants calculated from the fit were 3.93 ± 0.02 Å and 3.95 ± 0.02 Å for the Pt and Pd components, respectively. Table 1 shows that the Pt fit value closely matches the bulk Pt lattice parameter. Conversely, the Pd data show a 1.5% dilation of the lattice parameter compared to the literature value of 3.89 Å. This tensile strain was also found in the Pd microscopy and XRD derived lattice constants (Table 1) though of varying magnitude. Like Ag in the Au–Ag samples, Pd now adopts an extended, ordered habit instead of an amorphous one. PDF fit results indicated a mean particle diameter of 2.1 ± 0.2 nm. Inclusion of the low-*Z* component when measuring the average size with microscopy gives a size of 20.7 ± 8.2 nm for the Pt–Pd nanostructures which is nearly an order of magnitude larger. This value does however closely approximate that of the high-*Z* Pt cluster core (3.5 ± 1.4 nm, Figure 7b).

The discrepancies in the bimetallic cluster sizes predicted for both Au–Ag and Pt–Pd when using C_s-STEM and PDF modeling are unexpected. There are two likely reasons why discrepancies of this sort might arise. First, if part of the structure lacks order it will present a broadened (and for this reason difficult to distinguish) signal in the PDF analysis, even for large nanocrystals. Given that the 2M metal shells appear in the C_s-STEM data to have structures that are very similar to the 3M cores, this prospective complication can be safely discounted. The second reason that the 2M metal shell might not contribute to the cluster size determined by the PDF analysis is if bonding present in the shell contributes a much smaller fraction of bonds at a given distance relative to those present in the 3M core. To investigate this possibility we carried out additional quantitative analyses of the binary crystal C_s-STEM micrographs.

Structural Analysis of Binary Nanocrystals. The atomic strains evidenced in the structure of the 2M metal components for the bimetallic samples of Au–Ag and

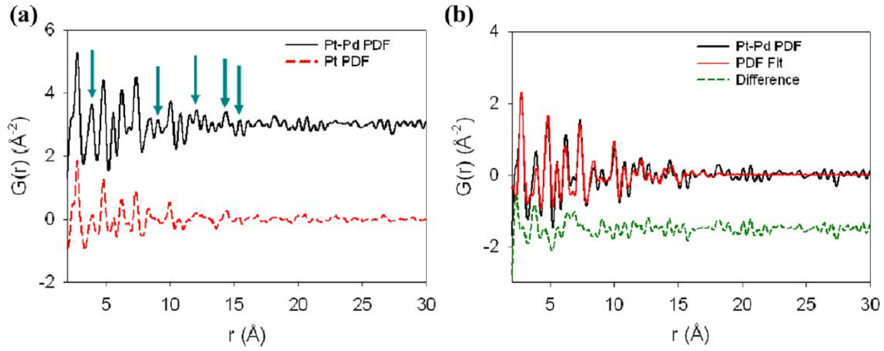

Figure 9. (a) Comparison of the atomic PDFs for the bimetallic Pt–Pd (vertically displaced by +3 Å^{-2}) and the monometallic Pt samples. Arrows in the bimetallic PDF highlight the emergence of atom-pair contributions unaccounted for in the monometallic Pt profile. (b) The experimental PDF data for the Au–Ag nanocrystals (in black) is modeled (in red) with a difference profile also shown (in green, vertically displace by −1.5 Å^{-2}).

Pt–Pd warrant further discussion. The atomic PDF analysis of the Au–Ag system indicated a particle size of 5.35 ± 0.2 nm. As mentioned above, this value was only appropriate if the particle dimensions were defined by the Au component of the nanostructure. To determine why structures synthesized using a 1:1 ratio of Au to Ag—and presenting such an extended structure—had such unusual behavior, an atom quantification study was conducted on these samples.

The intensity (*I*) observed in C_s-STEM micrographs is produced from an atomic volume (*V*) by a number of atoms (*N*) projected onto an image. This intensity scales with atomic number ($\sim Z^{1.6}$) such that,[61]

$$N_X \times V_X \times Z_X^{1.6} = \frac{I}{K}$$

where X represents a particular atomic species and *K* is a constant of proportionality. If we consider the high-contrast region to isotropically fill three-dimensions we can correlate the diameter to an approximate number of atoms. This was done by calculating the dependence of the number of atoms with respect to the diameter (S.I. Figure 10) of the monometallic Au nanocrystals (Figure 1a–c) as outlined in a previous work.[46] In doing so, we are able to correlate an atom count to an expected particle diameter. With N_{Au}, the volume of a Au atom (V_{Au} where $V_X = 4/3\pi r^3$ and $r = 0.135$ nm for the radius of a Au (or Pt) atom), and the measured *I* in place, N_{Ag} can be determined by equating

$$\frac{I_{Au}}{N_{Au} \times V_{Au} \times Z_{Au}^{1.6}} = \frac{I_{Ag}}{N_{Ag} \times V_{Ag} \times Z_{Ag}^{1.6}}$$

where the volume of a Ag atom (V_{Ag}; where $r = 0.160$ nm (0.140 nm) for the Ag (Pd) atom) and atomic number (*Z*; where $Z_{Au} = 79$, $Z_{Pt} = 78$, $Z_{Ag} = 47$, and $Z_{Pd} = 46$) can be obtained using literature values. The value for I_{Ag} can be determined by integrating the intensity from a region containing the low-*Z* component as seen in S.I. Figure 11a. Once calculated, N_{Ag} provides a scaled numerical value representing the same total volume encompassed by the integrated area. With proper background subtraction this provides a comparative method of determining whether or not the exhibited intensities are demonstrative of a similar number of atoms. The comparison can then be expanded so that aspects of structure can be inferred.

For the Au–Ag sample it was consistently found that the volume of intensity for the high intensity regions (presumably Au) encompassed a greater number of atoms than the low intensity regions (presumably Ag). This may seem intuitive as the stronger scattering Au atoms would have a greater likelihood of generating a signal into the dark-field detector. However, this highlights the significance of scaling the results by the atomic number ($Z^{1.6}$) to account for the difference in scattering power of the two elements.[61] We have thus accounted for differences in the scattering strength as the source in variation between N_{Au} and N_{Ag} and present our estimates in Table 2 (N_{Pt} and N_{Pd} in Table 3). The considerable drop in atom count (going from N_{Au} to N_{Ag}) means that there are less Ag atoms inhabiting the same volume as the Au core. On the basis of the data in Table 2 we infer that the Ag atoms must adopt a low aspect ratio structure, projecting from a facet of the pre-existing Au nanocrystal (top right inset, Figure 7a). Incidentally, Figure 7a shows the presence of a twin boundary on the Au nanocrystal from which the Ag atom growth propagates. Although a more globular morphology might be expected for a solution-based synthesis, it should be noted that both Au and Ag have been shown to form nanoplates under certain growth conditions.[22] In contrast, analysis of the Pt–Pd nanostructures (S.I. Figure 11b) shows growth that appears to be more globular; with the Pd sites nucleating more heterogeneously on the Pt core cluster.

TABLE 2. Comparison of the Calculated Number of Ag Atoms to Those Determined for Au for Measured Nanoparticle. The Measured Particle Size Was Determined from the High-*Z* Component of the Binary Structures

	atom quantification for the binary Au–Ag system	
measured particle size (nm)	no. of Au atoms, N_{Au}	calcd no. of Ag atoms, N_{Ag}
2.68	1250	394
3.75	2200	1450
3.84	2700	888
4.7	5400	1511
5.2	8300	5245
5.45	8700	2336

TABLE 3. Comparison of the Calculated Number of Pd Atoms to Those Determined for Pt for Measured Nanoparticle. The Measured Particle Size Was Determined from the High-*Z* Component of the Binary Structures

	atom quantification for the binary Pt–Pd system	
measured particle size (nm)	no. of Pt atoms, N_{Pt}	calcd no. of Pd atoms, N_{Pd}
2.2	680	2696
2.65	700	915
4.3	3000	2015
5.3	4600	3168
5.94	5000	3033
6.55	7000	4102

Analysis of Contributions to Nanoparticle Shape. When considering the degree of crystallinity exhibited by nanoparticles, various factors are frequently implicated for the final structure observed. Some common reasons given for an observed morphology are the reduction rate, the stacking fault energy of the metal, the surface energy of the metal, and/or the presence of adsorbates. In the first case, the reduction will yield more amorphous/twinned particles or single

TABLE 4. Reduction Potentials for Ions from the Metal Salts Used in This Study[a]

reaction	reduction potential (eV)
$BH_4^- + 8OH^- \leftrightarrow H_2BO_3^- + 5H_2O + 8e$	1.24
$AuCl_4^- + 3e \leftrightarrow Au + 4Cl^-$	1.002
$Ag^+ + e \leftrightarrow Ag$	0.7996
$IrCl_6^{2-} + e \leftrightarrow IrCl_6^{3-}$	0.8665
$IrCl_6^{3-} + 3e \leftrightarrow Ir + 4Cl^-$	0.77
$PtCl_6^{2-} + 2e \leftrightarrow PtCl_4^{2-} + 2Cl^-$	0.68
$PtCl_4^{2-} + 2e \leftrightarrow Pt + 2Cl^-$	0.755
$PdCl_4^{2-} + 2e \leftrightarrow Pd + 4Cl^-$	0.591
$RhCl_6^{3-} + 3e \leftrightarrow Rh + 6Cl^-$[b]	0.431

[a] All data were obtained from: Lide, D. R. *CRC Handbook of Chemistry and Physics*, 87th ed.; CRC Press: Boca Raton, FL, 2006. [b] $RhCl_3$ has multiple hydrated forms when in aqueous solution. The form given is one of the most common.

crystalline particles depending on the degree of kinetic control.[22,23] The relative importance of kinetic formation *versus* thermodynamic stability should be reflected in how quickly the different metals are reduced.[23] Reduction potentials for the various metal ion reactants are given in Table 4.[45] A ranking of the reduction potentials that result in a metallic state gives the relative order: Au > Ag > Ir > Pt > Pd > Rh. From this it can be seen that the 3M metal atoms tend to have a higher reduction potential and are therefore expected to nucleate more quickly than the 2M metal atoms. Consequently, it would be expected that they would also be the structures most impacted by kinetics and form an array of structures. As the data above show, this is not the case.

A second possible cause for the observed trends is the stacking fault energies of the metals. Pt has a high stacking fault energy (322 mJ/m^2) and is 280 mJ/m^2 higher than that of Au (42 mJ/m^2);[62] meaning that a higher energetic cost would be required to induce a dislocation/deformation process in a Pt crystal. This can explain why Au is seen to produce symmetrically twinned structures in particles as large as ~6 nm (S.I. Figure 2). Somewhat oddly, the stacking fault energy of Ir (480 mJ/m^2)[62] is significantly higher than that of Pt, making it more energetically costly to introduce structural imperfections into the Ir lattice despite our observation that twinning becomes more common at larger sizes. Similarly, the qualitative features seen for the Ag clusters can be explained by the relatively low stacking fault energy of Ag (20 mJ/m^2, lowest among all the metals examined here) when compared to Rh (750 mJ/m^2) and Pd (180 mJ/m^2).[62] Not only does the stacking fault energy of Rh exceed that of Pd, but it also does so for all of the other metals investigated (S.I. Figure 13). Yet Figure 2 shows that the 580 mJ difference in stacking fault energy (between Rh and Pd) does not lead to markedly dissimilar nanostructures. While stacking fault energies might underpin some of our observations, there clearly remain other factors that can contribute to the degree of disorder present within a nanocluster.

That leads us to consider the role that surface energies may play in dictating the final structure. Both experimental[34,63] and theoretical[34] evidence confirm that the intracolumn surface energies (where surface energy is defined as the energy required to create a surface)[22] of the 2M metals are lower than those of their intracolumn 3M counterparts (S.I. Figure 14). For example, the experimentally determined surface energy for the (111) surface of Au is 1.506 J/m^2, a value greater than that of the 1.246 J/m^2 found for (111) Ag.[63] Related differences in physical properties have also been documented in comparisons made between Pt and Pd (2.489 and 2.003 J/m^2, respectively)[63] and between Ir and Rh (3.048 and 2.659 J/m^2, respectively).[63] Theoretical studies have further extended these trends to the (100) and (110) surfaces where it has been convincingly established that the 3M specimens consistently have higher surface energies than their 2M counterparts.[34] It is interesting to note that the metal with the highest surface energies (Ir, *e.g.*, 3.048 J/m^2 for the (111) plane) readily overcomes the energetic barrier to the formation of facets, whereas the metal with the lowest surface energies (Ag, *e.g.*, 1.246 J/m^2 for the (111) plane) does not. Although the properties of nanomaterials will undoubtedly differ from those in a bulk state, we think it reasonable to presume that the surface energy trends will maintain their relative order even in the nanoregime. This is an important point as, to some degree, it mitigates the argument that the difference in lattice structure between the 2 and 3M nanoparticles is entirely driven by surface energetics. If this is the case, surface energetics alone cannot entirely explain the variances in crystallinity observed.

Lastly, in view of the noted effects of heteroepitaxy, the role of adsorbed species on the structures observed herein must also be taken into consideration.[18] For instance, it has been shown that the chemisorption of O_2 can result in the expansion of the lattice parameter for Ag.[64] The introduction of an adsorbed species would likely reduce the surface energy required to distort/expand the relative atom pair distances.[64] Adsorbed species could be used to explain the disorder exhibited by some of the nanocrystals except that, in the presence of a secondary metal, such disorder was absent in several cases. As can be strongly inferred from the data in Figure 7a and b, adsorbed species cannot be responsible for the morphology of the particles formed.

What then is the origin of the mesoscopic structural dichotomy between the 2 and 3M particles? We believe that the differences seen in the metal-atom bonding reflect impacts on electronic structure due to relativistic effects. Briefly recounted, the inner electrons of heavy elements experience a large nuclear charge such that they must reach levels approaching the speed of light to sustain a balance with the embedded, electrostatic potential. The acceleration results in an increase in the electron's relativistic mass and contraction of the 1s orbital.[65] These effects propagate such that they lead to a contraction of the 6s orbital, an expansion of the 5d orbitals and, consequently, impacting the use of the 5d electrons for the purposes of bonding.[65] This difference in bonding nature does not necessarily reflect a difference in bond strength; rather, it serves to rationalize the tendency for the 3M metal atoms to undergo directional bonding. This would then establish a correlation with the barrier heights associated with metal atom placements occurring at locally high symmetry (*i.e.*, directional) or more disordered sites. The correlations suggested here have in fact been used by others to account for the ground-state energetics of both nano- and surface-structural features. Regarding the former cases, experimental[4,66] observations and theoretical calculations[67] invoking relativistic effects explain why atomic chains of the 3M metals can be formed while ones comprising metals of the 2M series cannot. Relativistic effects have also been used to explain the complex dynamics evidenced in surface reconstructions. Most notable in this regard are the now well established motifs seen in the reconstruction of the (110) and (111) facets of 3M metal crystals—structural behaviors not evidenced in crystals of the 2M metals.[65,68]

When taken together, the current results suggest that the presence of a 3M metal atom can be used to impart its patterns of bonding to other metal atoms. This strongly implicates that the critical barriers for growth in ordered habits are strongly tied to the electronic structure, and, hence, the surface and twinning energies of the 3M atoms present. Referring back to Figure 2a–c as an exemplary case, we note the disordered structural behaviors seen in monometallic Ag nanoclusters (where both atomic PDF measurements and microscopy results both confirmed the lack of a defined crystal structure for these clusters). Introducing Au into the reaction induced (locally) ordered Ag–Ag bonding that propagates more than 5 nm beyond the critical nucleus (inset of Figure 7a). A similar pattern of order being imparted onto a growing 2M metal cluster by a 3M metal is also seen in the Pt–Pd bimetallic sample (Figure 7b). Although the bimetallic samples possess sizes larger than the range of monometallic samples investigated, the epitaxial growth exhibited here has also been observed for both bulk-like Pt–Pd structures in work by Habas *et al.*[1] and in 2–4 nm Pt–Pd nanoparticles by Sanchez, *et al.*[46] Indeed, the latter work also revealed instances of nonuniform growth dependent upon the nucleation center. In light of the present work, we can posit that the structures seen in those works were driven by the higher surface and stacking fault energies of Pt even in the case where the shell layer was Pt. At the small sizes that we have examined, this templating appears to be true irrespective of whether the system is formed *via* thermodynamic or kinetic control.

CONCLUSIONS

This study presents information regarding the dynamics of metal atom bond formation in nanoscale materials growth. We note trends that distinguish the nanostructures formed by second and third row, fcc, transition metal series. Complex physicochemical effects underpin the formation of the distinct bonding motifs seen. The present data strongly suggest that the 3M metals function far more effectively in imparting ordered bonding characteristics than their 2M counterparts through relativistic effects that manifest themselves as surface and stacking fault energies. Specifically, the intrinsic electronic nature of Au, Pt, and Ir atoms promotes a more uniform bonding network that is sustained by additional growth species even if their natural state is more disordered. What remains unclear, at present, is the size of the critical nucleus that might be involved in this regard: the number of metal atoms that need be present in a cluster and how the complex solution phase environment comprising the growth media might serve to perturb/stabilize these structures. It remains an interesting and particular challenge to develop experimental means to explore the structural dynamics of metal atom clusters of this size at atomic resolution in the complex (and evolving) chemical environments as are found in the nucleation processes mediating growth.

Finally we note that the results reported here have important implications beyond crystal growth. Most notably, the complex nature of the bond strains seen in metal clusters of varied form (and significant deviations from bulk bonding habits) might lead to correlated impacts on the energetics of reactions carried out using materials of this form as catalysts. Such features remain very poorly understood within the current literature and form, we believe, an important forward going opportunity for future progress in research.

EXPERIMENTAL METHODS

Preparation of Nanocrystals. $HAuCl_4$ (FW = 339.79 g/mol), $RhCl_3$ (FW = 209.26 g/mol), and $H_2PtCl_6 \cdot 6H_2O$ (FW = 517.92 g/mol) were purchased from Strem Chemicals. The $H_2IrCl_6 \cdot 6H_2O$ (FW = 406.93 g/mol), $AgNO_3$ (FW = 169.8 g/mol), Na_2PdCl_4 (FW = 294.19 g/mol) precursors, polyvinylpyrrolidone (PVP; FW = 40 000 g/mol) and reagent grade $NaBH_4$ (FW = 37.83 g/mol) were purchased from Sigma-Aldrich.

The protocol used to produce the nanocrystals was adapted from the work of Tsunoyama *et al.*[56] To summarize, a typical reaction began by chilling a 0.3 mM solution of PVP in deionized water (∼50 mL) to 0 °C using an ice bath. To this solution was added 0.05 mmol of the desired metal precursor. The subsequent solution was purged with N_2 (g) for 30 min under vigorous magnetic stirring. A separate 5 mL solution of 0.1M $NaBH_4$ (aq) was prepared and rapidly added to the existing PVP/H_2O/metal precursor solution. The system was then allowed to react for 1 h while being maintained at 0 °C with N_2 (g) bubbling. Following synthesis, the solvent was evaporated, the samples dried, and then resuspended in ethanol and stored at ambient conditions.

In the case of the bimetallic samples the synthetic approach was unchanged with the exception that the two separate metals were simultaneously introduced into the reaction vessel. In place of the 0.05 mmol addition of one metal precursor, two 0.025 mmol equivalents of each of the different metal precursors were added to the chilled 0.3 mM PVP/H_2O solution.

Electron Microscopy. C_s-STEM samples were prepared by the dropwise addition of the prepared nanoparticle suspensions onto ultrathin holey carbon films supported on Cu-framed grids (Ted Pella, Inc.). C_s-STEM images were collected on a JEOL model 2200FS electron microscope operated at 200 keV capable of sub-angstrom resolution.[69] To prevent localized buildup of carbonaceous species (also known as "contamination") the beam was defocused by lowering the sample height as far as possible and the sample was irradiated at low magnification for ∼30 min before acquiring images for each sample. The inner-cutoff angle of the annular dark-field detector at a 60 cm camera length was 100 mrad, to ensure that no diffracted beams would interfere with the measured images. A 20 or 30 μm aperture was generally used during image acquisition to minimize the damage due to excessive radiation exposure. These aperture sizes limited the beam current to 13 and 30 pA, respectively. Additionally, the fast Fourier transform (FFT) of low magnification ($\sim 1.0 \times 10^6$ times magnification, S.I. Figure 12a) images were compared to the FFT of high magnification (15.0×10^6 times magnification, S.I. Figure 12b) images prior to image capture as a precautionary step to prevent the possibility of confusing beam-induced restructuring with the as-prepared structure of the nanocrystals. The microscope was also supplied with an Oxford INCA ATW detector (40 mm^2) for chemically sensitive energy dispersive X-ray spectroscopy measurements.

High-resolution STEM image evaluation, FFT, or power spectrum analysis, approximation of lattice parameters, and size distribution histograms were done using DigitalMicrograph (Gatan Inc.) software. Zone axis assignments were determined by measuring the ratio of the different spatial frequencies attendant within a FFT of a micrograph and comparing them to the diffraction patterns of an fcc crystal. After establishing crystal orientation the spatial frequencies were subsequently used to index and annotate the crystal planes on the corresponding micrograph. Mean lattice parameters were calculated by using the average distances measured from the central peak to a particular spatial frequency and evaluated with respect to the indexed crystal planes. Particles sizes were determined by measuring the diameter cross-section of many individual nanoparticles.

5.2.3. High-Energy X-ray Data Collection. For the monometallic samples, X-ray total scattering measurements were carried out at beamline 11-IDC at the Advanced Photon Source (APS), Argonne National Laboratory (ANL), with high energy X-rays (E_0 = 114.82 keV, λ = 0.108 Å) using the rapid acquisition mode.[70] The setup utilized a 2-D image plate detector (Perkin-Elmer) positioned perpendicular to the beam path 297.14 mm away from the mounted samples. Ethanol suspensions of the nanocrystals were sealed in cylindrical kapton capillary tubes (Cole-Palmer) 1 mm in diameter. The data were collected at 300 K. The exposure time was set for 250 s for each sample.

The bimetallic samples were collected at beamline X-7B at the National Synchrotron Light Source (NSLS), Brookhaven National Laboratory (BNL), with high-energy X-ray (E_0 = 38.94 keV, λ = 0.3184 Å), utilizing a 2-D image plate detector (Perkin-Elmer). The detector was placed orthogonal to the beam path at distance 116.18 mm away from the mounted samples. These ethanol-suspended samples were loaded in kapton cylindrical tubes measuring 1 mm in diameter. Owing to the lower flux of the X-ray radiation at beamline X-7B, exposure time was set for 900 s to improve the statistics of the collected data.

In both sets of experiments blank tubes (kapton) and tubes containing ethanol were simultaneously submitted for measurement for purposes of background removal.

X-ray Diffraction Analysis. For XRD analysis, the normalized, integrated data were examined without being sine Fourier transformed. Peak positions were identified using the radiation energy (λ = 0.108 Å), Bragg's law,

$$\lambda = 2d\sin\theta$$

and the inverse relationship in an fcc solid between the lattice constant, *a*, and interplanar distances, *d*

$$d = \frac{a}{\sqrt{h^2 + k^2 + l^2}}$$

where *h*, *k*, and *l* are the Miller indices of the corresponding Bragg planes. The *h*, *k*, and *l* values were determined by assignment of the spatial frequencies in the acquired power spectra.

Atomic Pair Distribution Function Analysis. The raw 2D data were integrated and converted to intensity *versus* 2θ using the software Fit2D,[71] with 2θ as the angle of diffraction. The integrated data were corrected for experimental artifacts, normalized, and sine Fourier transformed to the PDF, *G*(*r*), based on standard methods[54] using the program PDFgetX2.[72] Modeling was performed using the PDFgui program.[73] The upper limit in the Fourier transform, Q_{MAX} = 20.0 Å^{-1}, was optimized to avoid large termination effects and to reasonably minimize the introduction of noise. This was critical since the signal-to-noise ratio decreases with increasing *Q*.

Conflict of Interest: The authors declare no competing financial interest.

Acknowledgment. This work was sponsored in part by the United States Department of Energy Grant No. DE-FG02-03ER15476. Experiments were conducted in part at the Frederick Seitz Materials Research Laboratory Central Facilities, University of Illinois at Urbana−Champaign, which is partially supported by the United States Department of Energy under Grand Nos. DE-FG02-07ER46453 and DE-FG02-07ER46471. Work at Brookhaven National Laboratory, which is operated for the U.S. Department of Energy by Brookhaven Science Associates, is supported by Grant No. DE-AC02-98CH10886. Research was also carried out at the Advanced Photon Source (APS) at Argonne National Laboratory. Use of APS was supported by the United States Department of Energy, Office of Science, Office of Basic Energy Sciences, under Grant No. DE-AC02-06CH11357

Supporting Information Available: Additional information was referred to at various points in the text (*e.g.*, additional micrographs mentioned in the body of the text, energy dispersive X-ray spectra, size distribution histograms, and methodologies used to synthesize the high temperature noble metal nanoparticles). This material is available free of charge *via* the Internet at http://pubs.acs.org.

REFERENCES AND NOTES

1. Habas, S.; Lee, H.; Radmilovic, V.; Somorjai, G. A.; Yang, P. Shaping Binary Metal Nanocrystals through Epitaxial Seeded Growth. *Nature* **2007**, *6*, 692–697.
2. Lee, H.; Habas, S. E.; Kweskin, S.; Butcher, D.; Somorjai, G. A.; Yang, P. Morphological Control of Catalytically Active Platinum. *Angew. Chem., Int. Ed.* **2006**, *45*, 7824–7828.
3. Narayanan, R.; El-Sayed, M. A. Catalysis with Transition Metal Nanoparticles in Colloidal Solution: Nanoparticle Shape Dependence and Stability. *J. Phys. Chem. B* **2005**, *109*, 12663–12676.
4. Ohnishi, H.; Kondo, Y.; Takayanagi, K. Quantized Conductance through Individual Rows of Suspended Gold Atoms. *Nature* **1998**, *395*, 780–783.
5. Rao, C. N. R.; Sood, A. K.; Subrahmanyam, K. S.; Govindaraj, A. Graphene: The New Two-Dimensional Nanomaterial. *Angew. Chem., Int. Ed.* **2009**, *48*, 7752–7777.

6. Gao, H.; Ji, B.; Jager, I. L.; Artz, E.; Fratzl, P. Materials Become Insensitive to Flaws at Nanoscale: Lessons from Nature. *Proc. Natl. Acad. Sci. U.S.A.* **2003**, *100*, 5597–5600.
7. Nel, A. E.; Madler, L.; Velegol, D.; Xia, T.; Hoek, E. M. V.; Somasundaran, P.; Klaessig, F.; Castranova, V.; Thompson, M. Understanding Biophysicochemical Interactions at the Nano-Bio Interface. *Nature* **2009**, *8*, 543–557.
8. Rogers, J. A.; Lagally, M. G.; Nuzzo, R. G. Synthesis, Assembly and Applications of Semiconductor Nanomembranes. *Nature* **2011**, *477*, 45–53.
9. Roder, H.; Hahn, E.; Brune, H.; Bucher, J.-P.; Kern, K. Building One- and Two-Dimensional Nanostructures by Diffusion-Controlled Aggregation at Surfaces. *Nature* **1993**, *366*, 141–143.
10. Brune, H.; Giovannini, M.; Bromann, K.; Kern, K. Self-Organized Growth of Nanostructure Arrays on Strain-Relief Patterns. *Nature* **1998**, *394*, 451–453.
11. Goldberger, J.; He, R.; Zhang, Y.; Lee, S.; Yan, H.; Choi, H.-J.; Yang, P. Single-Crystal Gallium Nitride Nanotubes. *Nature* **2003**, *422*, 599–602.
12. Tian, Z. R.; Voigt, J. A.; Liu, J.; Mckenzie, B.; Mcdermott, M. J. Biomimetic Arrays of Oriented Helical ZnO Nanorods and Columns. *J. Am. Chem. Soc.* **2002**, *124*, 12954–12955.
13. Marks, L. D. Experimental Studies of Small Particle Structures. *Rep. Prog. Phys.* **1994**, *57*, 603–649.
14. Sato, K.; Huang, W. J.; Bohra, F.; Sivaramakrishnan, S.; Tedjasaputra, A. P.; Zuo, J. M. Size-Dependent Structural Transition from Multiple-Twinned Particles to Epitaxial fcc Nanocrystals and Nanocrystal Decay. *Phys. Rev. B* **2007**, *76*, 144113.
15. Bratlie, K. M.; Lee, H.; Komvopoulos, K.; Yang, P.; Somorjai, G. A. Platinum Nanoparticle Shape Effects on Benzene Hydrogenation Selectivity. *Nano Lett.* **2007**, *7*, 3097–3101.
16. Chen, J.; Lim, B.; Lee, E.; Xia, Y. Shape-Controlled Synthesis of Platinum Nanocrystals for Catalyic and Electrocatalytic Applications. *Nano Today* **2009**, *4*, 81–95.
17. Narayanan, R.; Tabor, C.; El-Sayed, M. A. Can the Observed Changes in the Size or Shape of a Colloidal Nanocatalyst Reveal the Nanocatalysis Mechanism Type: Homogeneous or Heterogeneous? *Top. Catal.* **2008**, *48*, 60–74.
18. An, K.; Somorjai, G. A. Size and Shape Control of Metal Nanoparticles for Reaction Selectivity in Catalysis. *ChemCatChem.* **2012**, *4*, 1512–1524.
19. Huang, W. J.; Sun, R.; Tao, J.; Menard, L. D.; Nuzzo, R. G.; Zuo, J. M. Coordination-Dependent Surface Atomic Contraction in Nanocrystals Revealed by Coherent Diffraction. *Nat. Mater.* **2008**, *7*, 308–313.
20. Sanchez, S.I.; Small, M. W.; Sivaramakrishnan, S.; Wen, J. G.; Zuo, J. M.; Nuzzo, R. G. Visualizing Materials Chemistry at Atomic Resolution. *Anal. Chem.* **2010**, *82*, 2599.
21. Sanchez, S.I.; Menard, L. D.; Bram, A.; Kang, J. H.; Small, M. W.; Nuzzo, R. G.; Frenkel, A. I. The Emergence of Nonbulk Properties in Supported Metal Clusters: Negative Thermal Expansion and Atomic Disorder in Pt Nanoclusters Supported on $\Gamma-Al_2O_3$. *J. Am. Chem. Soc.* **2009**, *131*, 7040.
22. Xia, Y.; Xiong, Y.; Lim, B.; Skrabalak, S. E. Shape-Controlled Synthesis of Metal Nanocrystals: Simple Chemistry Meets Complex Physics? *Angew. Chem., Int. Ed.* **2009**, *48*, 60–103.
23. Tao, A. R.; Habas, S.; Yang, P. Shape Control of Colloidal Metal Nanocrystals. *Small* **2008**, *4*, 310–325.
24. Henry, C. R. Morphology of Supported Nanoparticles. *Prog. Surf. Sci.* **2005**, *80*, 92–116.
25. Huang, X.; Tang, S.; Mu, X.; Dai, Y.; Chen, G.; Zhou, Z.; Ruan, F.; Yang, Z.; Zheng, N. Freestanding Palladium Nanosheets with Plasmonic and Catalytic Properties. *Nat. Nanotechnol.* **2011**, *6*, 28–32.
26. Jiang, H.-L.; Akita, T.; Ishida, T.; Haruta, M.; Xu, Q. Synergistic Catalysis of Au@Ag Core-Shell Nanoparticles Stabilized on Metal−Organic Framework. *J. Am. Chem. Soc.* **2011**, *133*, 1304–1305.
27. Shao, M. H.; Huang, T.; Liu, P.; Zhang, J.; Sasaki, K.; Vukmirovic, M. B.; Adzic, R. R. Palladium Monolayer and Palladium Alloy Electrocatalysts for Oxygen Reduction. *Langmuir* **2006**, *22*, 10409–10415.
28. Negreiros, F. R.; Soares, E. A.; de Carvalho, V. E. Energetics of Free Pure Metallic Nanoclusters with Different Motifs by Equivalent Crystal Theory. *Phys. Rev. B* **2007**, *76*, 205429−1/205429−11.
29. Mays, C. W.; Vermaak, J. S.; Wilsdorf, D. K. On Surface Stress and Surface Tension: II. Determination of the Surface Stress of Gold. *Surf. Sci.* **1968**, *12*, 134–140.
30. Vermaak, J. S.; Mays, C. W.; Kuhlmann-Wilsdorf, D. On Surface Stress and Surface Tension: I. Theoretical Calculations. *Surf. Sci.* **1968**, *12*, 128–133.
31. Callister, W. *Materials Science and Engineering—An Introduction*, 7th ed. ed.; Wiley: New York, 2006; p 84.
32. Stokes, R. J.; Evans, D. F. *Fundamentals of Interfacial Engineering*; Wiley-VCH: New York, 1997.
33. Van Hove, M. A.; Tong, S. Y. *The Structure of Surfaces*; Springer: New York, 1985; p 435.
34. Vitos, L.; Ruban, A. V.; Skriver, H. L.; Kollar, J. The Surface Energy of Metals. *Surf. Sci.* **1998**, *411*, 186–202.
35. Yang, Y.; Matsubara, S.; Xiong, L.; Hayakawa, T.; Nogami, M. Solvothermal Synthesis of Mulitple Shapes of Silver Nanoparticles and Their SERS Properties. *J. Phys. Chem. C* **2007**, *111*, 9095–9104.
36. Zhu, J.; Shen, Y.; Xie, A.; Qiu, L.; Zhang, Q.; Zhang, S. Photoinduced Synthesis of Anisotropic Gold Nanoparticles in Room-Temperature Ionic Liquid. *J. Phys. Chem. C* **2007**, *111*, 7629–7633.
37. Templeton, A. C.; Chen, S.; Gross, S. M.; Murray, R. W. Water-Soluble, Isolable Gold Clusters Protected by Tiopronin and Coenzyme a Monolayers. *Langmuir* **1999**, *15*, 66–76.
38. Frenkel, A. I.; Nemzer, S.; Pister, I.; Soussan, L.; Harris, T.; Sun, Y.; Rafailovich, M. H. Size-Controlled Synthesis and Characterization of Thiol-Stabilized Gold Nanoparticles. *J. Chem. Phys.* **2005**, *123*, 184701−1−184701−6.
39. Teranishi, T.; Hosoe, M.; Miyake, M. Formation of Monodispersed Ultrafine Platinum and Their Electrophoretic Deposition on Electrodes. *Adv. Mater.* **1997**, *9*, 65–67.
40. Baker, L. R.; Kennedy, G.; Krier, J. M.; Van Spronsen, M.; Onorato, R. M.; Somorjai, G. A. The Role of an Organic Cap in Nanoparticle Catalysis: Reversible Restructuring of Carbonaceous Material Controls Catalytic Activity of Platinum Nanoparticles for Ethylene Hydrogenation and Methanol Oxidation. *Catal. Lett.* **2012**, *142*, 1286–1294.
41. Dykeman, R. R.; Yuan, Y.; Yan, N.; Asakura, H.; Teramura, K.; Tanaka, T.; Dyson, P. J. Rational Design of a Molecular Nanocatalyst-Stabilizer That Enhances Both Catalytic Activity and Nanoparticle Stability. *ChemCatChem.* **2012**, *4*, 1907–1910.
42. Krier, J. M.; Michalak, W. D.; Baker, L. R.; An, K.; Komvopoulos, K.; Somorjai, G. A. Sum Frequency Generation Vibrational Spectroscopy of Colloidal Platinum Nanoparticle Catalysts: Disordering *versus* Removal of Organic Capping. *J. Phys. Chem. C* **2012**, *116*, 17540–17546.
43. Peng, Z.; Yang, H. Synthesis and Oxygen Reduction Electrocatalytic Property of Pt-on-Pd Bimetallic Heteronanostructures. *J. Am. Chem. Soc.* **2009**, *131*, 7542–7543.
44. Grzelczak, M.; Perez-Juste, J.; Mulvaney, P.; Liz-Marzan, L. M. Shape Control in Gold Nanoparticle Synthesis. *Chem. Soc. Rev.* **2008**, *37*, 1783–1791.
45. *CRC Handbook of Chemistry and Physics.*, 75 ed.; CRC Press: Boca Raton, 1995.
46. Sanchez, S.; Small, M.; Zuo, J.-M.; Nuzzo, R. G. Structural Characterization of Pt−Pd and Pd−Pt Core−Shell Nanoclusters at Atomic Resolution. *J. Am. Chem. Soc.* **2009**, *131*, 8683–8689.
47. Yang, X. C.; Dubiel, M.; Brunsch, S.; Hofmeister, H. X-Ray Absorption Spectroscopy Analysis of Formation and Structure of Ag Nanoparticles in Soda-Lime Silicate Glass. *J. Non-Cryst. Sol.* **2003**, *328*, 123–136.
48. Sun, Y.; Frenkel, A. I.; Isseroff, R.; Shonburn, C.; Forman, M.; Shin, K.; Koga, T.; White, H.; Zhang, L.; Zhu, Y.; Rafailovich, M. H.; Sokolov, J. C. Characterization of Palladium Nanoparticles by Using X-ray Reflectivity, EXAFS, and Electron Microscopy. *Langmuir* **2006**, *22*, 807–816.
49. Lamber, R.; Wetjen, S.; Jaeger, N. I. Size Dependence of the Lattice Parameter of Small Palladium Particles. *Phys. Rev. B* **1995**, *51*, 10968–10971.

50. Teranishi, T.; Miyake, M. Size Control of Palladium Nanoparticles and Their Crystal Structures. *Chem. Mater.* **1998**, *10*, 594–600.
51. Jeon, Y. T.; Lee, G. H. Magnetism of the fcc Rh and Pd Nanoparticles. *J. Appl. Phys.* **2008**, *103*, 094313−1–094313−5.
52. Petkov, V.; Billinge, S. J. L.; Heising, J.; Kanatzidis, M. G. Application of Atomic Pair Distribution Function Analysis to Materials with Intrinsic Disorder. Three-Dimensional Structure of Exfoliated-Restacked Ws_2: Not Just a Random Turbostratic Assembly of Layers. *J. Am. Chem. Soc.* **2000**, *122*, 11571–11576.
53. Billinge, S. J. L.; Kanatzidis, M. G. Beyond Crystallography: The Study of Disorder, Nanocrystallinity and Crystallography Challenged Materials with Pair Distribution Functions. *Chem. Commun.* **2004**, 749–760.
54. Egami, T.; Billinge, S. J. L. *Underneath the Bragg Peaks: Structural Analysis of Complex Materials*; Pergamon Press: Oxford, 2003; Vol. 7.
55. Petkov, V.; Ohta, T.; Hou, Y.; Ren, Y. Atomic-Scale Structure of Nanocrystals by High-Energy X-ray Diffraction and Atomic Pair Distribution Function Analysis: Study of Fe_xpd_{100-X} ($X = 0, 26, 28, 48$) Nanoparticles. *J. Phys. Chem. C* **2007**, *111*, 714–720.
56. Tsunoyama, H.; Sakurai, H.; Negishi, Y.; Tsukuda, T. Size-Specific Catalytic Activity of Polymer-Stabilized Gold Nanoclusters for Aerobic Alcohol Oxidation in Water. *J. Am. Chem. Soc.* **2005**, *127*, 9374–9375.
57. Wiley, B.; Sun, Y.; Xia, Y. Synthesis of Silver Nanostructures with Controlled Shapes and Properties. *Acc. Chem. Res.* **2007**, *40*, 1067–1076.
58. Williams, D. B.; Carter, B. C. *Transmission Electron Microscopy: Basics*; Springer Science+Business Media Inc.: New York, 1996.
59. Rosenthal, S.; McBride, J.; Pennycook, S.; Feldman, L. Synthesis, Surface Studies, Composition and Structural Characterization of CdSe, Core/Shell and Biologically Active Nanocrystals. *Surf. Sci. Rep.* **2007**, *62*, 111.
60. Wang, J. X.; Inada, H.; Wu, L.; Zhu, Y.; Choi, Y.-M.; Liu, P.; Zhou, W.-P.; Adzic, R. R. Oxygen Reduction on Well-Defined Core−Shell Nanocatalysts: Particle Size, Facet, and Pt Shell Thickness Effects. *J. Am. Chem. Soc.* **2009**, *131*, 17298–17302.
61. Krivanek, O. L.; Chisholm, M. F.; Nicolosi, V.; Pennycook, T. J.; Corbin, G. J.; Dellby, N.; Murfitt, M. F.; Own, C. S.; Szilagyi, Z. S.; Oxley, M. P.; Pantelides, S. T.; Pennycook, S. J. Atom-by-Atom Structural and Chemical Analysis by Annular Dark-Field Electron Microscopy. *Nature* **2010**, *464*, 571.
62. Rosengaard, N. M.; Skriver, H. L. Calculated Stacking-Fault Energies of Elemental Metals. *Phys. Rev. B* **1993**, *47*, 12865–12873.
63. Tyson, W. R.; Miller, W. A. Surface Free Energies of Solid Metals: Estimation from Liquid Surface Tension Measurements. *Surf. Sci.* **1977**, *62*, 267–276.
64. Hu, J.; Cai, W.; Li, C.; Gan, Y.; Chen, L. *In Situ* X-ray Diffraction Study of the Thermal Expansion of Silver Nanoparticles in Ambient Air and Vacuum. *Appl. Phys. Lett.* **2005**, *86*, 151915−1–151915−3.
65. Bond, G. C. Relativistic Effects in Coordination, Chemisorption and Catalysis. *J. Mol. Catal. A* **2000**, *156*, 1–20.
66. Smit, R. H. M.; Untiedt, C.; Yanson, A. I.; van Ruitenbeek, J. M. Common Origin for Surface Reconstruction and the Formation of Chains of Metal Atoms. *Phys. Rev. Lett.* **2001**, *87*, 266102.
67. Bahn, S. R.; Jacobson, K. W. Chain Formation of Metal Atoms. *Phys. Rev. Lett.* **2001**, *87*, 266101.
68. Takeuchi, N.; Chan, C. T.; Ho, K. M. Reconstruction of the (100) Surfaces of Au and Ag. *Phys. Rev. B* **1991**, *43*, 14363–14370.
69. Wen, J.-G.; Mabon, J.; Lei, C. H.; Burdin, S.; Sammann, E.; Petrov, I.; Shah, A. B.; Chobpattana, V.; Zhang, J.; Ran, K.; Zuo, J.-M.; Mishina, S.; Aoki, T. The Formation and Utility of Sub-angstrom to Nanometer-Sized Electron Probes in the Aberration-Corrected Transmission Electron Microscope at the University of Illinois. *Microsc. Microanal.* **2010**, *16*, 183–193.
70. Chupas, P. J.; Qiu, X.; Hanson, J. C.; Lee, P. L.; Grey, C. P.; Billinge, S. J. L. Rapid Acquisition Pair Distribution Function Analysis (RA-PDF). *J. Appl. Crystallogr.* **2003**, *36*, 1342–1347.
71. Hammersley, A. P.; Svenson, S. O.; Hanfland, M.; Hauserman, D. Two-Dimensional Detector Software: From Real Detector to Idealised Image or Two-Theta Scan. *High Press. Res.* **1996**, *14*, 235.
72. Qiu, X.; Thompson, J. W.; Billinge, S. J. L. PDFgetX2: A Gui-Driven Program to Obtain the Pair Distribution Function from X-ray Powder Diffraction Data. *J. Appl. Crystallogr.* **2004**, *37*, 678.
73. Farrow, C. L.; Juhas, P.; Liu, J. W.; Bryndin, D.; Bozin, E. S.; Bloch, J.; Proffen, T.; Billinge, S. J. L. PDFfit2 and PDFgui: Computer Programs for Studying Nanostructure in Crystals. *J. Phys.: Condens. Matter* **2007**, *19*, 335219−1–335219−7.